Intraseasonal Variability Associated with Summer Precipitation over South America Simulated by 14 IPCC AR4 Coupled GCMs

JIA-LIN LIN,* TOSHIAKI SHINODA,+ BRANT LIEBMANN,# TAOTAO QIAN,*,@ WEIQING HAN,& PAUL ROUNDY,** JIAYU ZHOU,++ AND YANGXING ZHENG#

* *Department of Geography, The Ohio State University, Columbus, Ohio*
+ *Naval Research Laboratory, Stennis Space Center, Mississippi*
# *NOAA/ESRL/CIRES Climate Diagnostics Center, Boulder, Colorado*
@ *Byrd Polar Research Center, The Ohio State University, Columbus, Ohio*
& *Department of Atmospheric and Oceanic Sciences, University of Colorado, Boulder, Colorado*
** *University at Albany, State University of New York, Albany, New York*
++ *NOAA/NWS/OST, Silver Spring, Maryland*

(Manuscript received 2 September 2008, in final form 19 March 2009)

ABSTRACT

This study evaluates the intraseasonal variability associated with summer precipitation over South America in 14 coupled general circulation models (GCMs) participating in the Intergovernmental Panel on Climate Change (IPCC) Fourth Assessment Report (AR4). Eight years of each model's twentieth-century climate simulation are analyzed. Two dominant intraseasonal bands associated with summer precipitation over South America are focused on: the 40- and the 22-day band. The results show that in the southern summer (November–April), most of the models underestimate seasonal mean precipitation over central-east Brazil, northeast Brazil, and the South Atlantic convergence zone (SACZ), while the Atlantic intertropical convergence zone (ITCZ) is shifted southward of its observed position. Most of the models capture both the 40- and 22-day band around Uruguay, but with less frequent active episodes than observed. The models also tend to underestimate the total intraseasonal (10–90 day), the 40-, and the 22-day band variances. For the 40-day band, 10 of the 14 models simulate to some extent the 3-cell pattern around South America, and 6 models reproduce its teleconnection with precipitation in the south-central Pacific, but only 1 model simulates the teleconnection with the MJO in the equatorial Pacific, and only 3 models capture its northward propagation from 50° to 32°S. For the 7 models with three-dimensional data available, only 1 model reproduces well the deep baroclinic vertical structure of the 40-day band. For the 22-day band, only 6 of the 14 models capture its northward propagation from the SACZ to the Atlantic ITCZ. It is found that models with some form of moisture convective trigger tend to produce large variances for the intraseasonal bands.

1. Introduction

The climate of tropical South America is characterized by a pronounced summer monsoon, which is often referred to as the South American monsoon system (SAMS; Kousky 1988; Horel et al. 1989; Lenters and Cook 1995; Zhou and Lau 1998; see reviews by Nogués-Paegle et al. 2002; Vera et al. 2006a). The summer precipitation over South America has strong intraseasonal variability with the leading pattern of deep convection showing a seesaw between the South Atlantic convergence zone (SACZ) and the subtropical plains of South America (Nogués-Paegle and Mo 1997) Further studies show that this seesaw pattern is part of a much larger Rossby wave train structure that include alternating centers of negative and positive streamfunction, geopotential height, and temperature anomalies in the southern portion of the continent, and farther upstream in the southern Pacific (Liebmann et al. 1999, 2004; Paegle et al. 2000; Jones and Carvalho 2002; Diaz and Aceituno 2003; Carvalho et al. 2004). Using singular spectrum analysis, Paegle et al. (2000) found that this seesaw pattern is dominated by two frequency bands: a band with a period of about 36–40 days (hereafter the 40-day band) and a band with a period of about 22–28 days (hereafter the 22-day band). Both bands are linked to tropical convection. The 40-day band is related to the Madden–Julian oscillation (MJO) in the

Corresponding author address: Dr. Jia-Lin Lin, Department of Geography, The Ohio State University, 1105 Derby Hall, 154 North Oval Mall, Columbus, OH 43210.
E-mail: lin.789@osu.edu

DOI: 10.1175/2009MWR2777.1

tropics while the 22-day band is connected to a tropical mode at the corresponding frequency band. When the SACZ is enhanced, these two bands become meridionally aligned locally and such episodes are characterized by a wave train propagating northward from southern South America toward the tropics. These intraseasonal bands are responsible for alternating wet and dry episodes over the SAMS region. Few studies, however, have evaluated the simulations of the intraseasonal variability of the summer precipitation over South America by general circulation models (GCMs). Misra (2005) examined the simulation by one atmospheric GCM and found the intraseasonal variability to be inadequately represented. Furthermore, downscaling the GCM results to a regional model did not improve the variability.

Recently, in preparation for the Intergovernmental Panel on Climate Change (IPCC) Fourth Assessment Report (AR4), more than a dozen international climate modeling centers conducted a comprehensive set of long-term simulations for both the twentieth-century's climate and different climate change scenarios in the twenty-first century, which constitutes the third phase of the World Climate Research Programme (WCRP) Coupled Model Intercomparison Project (CMIP3; Meehl et al. 2007). This is an unprecedented, comprehensive coordinated set of global coupled climate experiments for the twentieth and twnty-first century. Before conducting the extended simulations, many of the modeling centers applied an overhaul to their physical schemes to incorporate state-of-the-art research results. For example, almost all modeling centers have implemented prognostic cloud microphysics schemes in their models, some have added a moisture trigger to their deep convection schemes, and some now take into account convective momentum transport. Moreover, many modeling centers increased their models' horizontal and vertical resolutions and some conducted experiments with different resolutions.

The purpose of this study is to evaluate the intraseasonal variability of precipitation associated with the summer precipitation over South America in 14 IPCC AR4 coupled GCMs, with emphasis on the 40- and the 22-day bands. While there has been some analysis of seasonal means of the IPCC runs in this region (e.g., Vera et al. 2006b), intraseasonal variability has not been studied. The models and validation datasets used in this study are described in section 2. The diagnostic methods and results are described in section 3. A summary and discussion are given in section 4.

2. Models and validation datasets

This analysis is based on 8 years of the climate of the twentieth century (20C3M) simulations from 14 coupled GCMs. Table 1 shows the model names and acronyms, their horizontal and vertical resolutions, and brief descriptions of their deep convection schemes. For each model we use 8 yr of daily mean surface precipitation. Three-dimensional data are available for 7 of the 14 models, for which we analyzed upper-air winds, temperature, and specific humidity.

The model simulations are validated using the Global Precipitation Climatology Project (GPCP) version 2 precipitation (Huffman et al. 2001). We use 8 yr (1997–2004) of daily data with a horizontal resolution of $1° \times 1°$. We also use 8 yr (1997–2004) of daily National Centers for Environmental Prediction–National Center for Atmospheric Research (NCEP–NCAR) reanalysis data (Reanalysis I; Kalnay et al. 1996), for which we analyzed upper-air winds, temperature, and specific humidity.

Total intraseasonal (periods of 10–90 days) anomalies were obtained by applying a 365-point 10–90-day Lanczos filter (Duchan 1979). Because the Lanczos filter is nonrecursive, 182 days of data were lost at each end of the time series (364 days in total). The dominant intraseasonal bands are determined using wavelet spectrum because they are active mainly during the southern summer. Wavelet spectrum is a powerful tool for analyzing multiscale, nonstationary processes, and can simultaneously determine both the dominant bands of variability and how those bands vary in time (e.g., Mak 1995; Torrence and Compo 1998). We utilize the wavelet analysis program developed by Torrence and Compo (1998) and use the Morlet wavelet as the mother wavelet. The 40-day band is defined as precipitation variability in the period range of 30–60 days, and was obtained by applying a 365-point 30–60-day Lanczos filter. Similarly, the 22-day band is defined as precipitation variability in the period range of 20–30 days, again using a 365-point Lanczos filter. We also tested the Murakami (1979) filter with similar results.

3. Results

a. Southern summer (November–April) seasonal mean precipitation

Previous observational studies indicate that the intraseasonal variance of precipitation is highly correlated with time-mean precipitation (e.g., Wheeler and Kiladis 1999). That is, areas with abundant mean precipitation tend to be characterized by large intraseasonal variability. Therefore, we first look at the horizontal distribution of southern summer (November–April) seasonal mean precipitation [Fig. 1; see also Vera et al. (2006b) for an evaluation of 3-month season climatologies of the IPCC

TABLE 1. List of models that participate in this study.

Modeling groups	IPCC ID (label in figures)	Grid type/resolution/model top	Deep convection scheme/modification	Downdrafts* SC/UC/Meso	Closure/ trigger
NOAA/GFDL	GFDL-CM2.0 (GFDL2.0)	Grid point 144/90/L24 3 mb	Moorthi and Suarez (1992)/Tokioka et al. (1988)	N/N/N	CAPE/threshold
NOAA/GFDL	GFDL-CM2.1 (GFDL2.1)	Grid point 144/90/L24 3 mb	Moorthi and Suarez (1992)/Tokioka et al. (1988)	N/N/N	CAPE/threshold
NCAR	CCSM3 (CCSM3)	Spectral T85/L26 2.2 mb	Zhang and McFarlane (1995)	Y/N/N	CAPE
NCAR	PCM (PCM)	Spectral T42/L26 2.2 mb	Zhang and McFarlane (1995)	Y/N/N	CAPE
NASA/GISS	GISS-AOM (GISS-AOM)	Grid point 90/60/L12	Russell et al. (1995)	N/N/N	CAPE
NASA/GISS	GISS-ER (GISS-ER)	Grid point 72/46/L20 0.1 mb	Del Genio and Yao (1993)	Y/N/N	Cloud base buoyancy
Center for Climate System Research, National Institute for Environmental Studies, and Frontier Research Center for Global Change	MIROC3.2(hires) (MIROC-hires)	Spectral T106/L56	Pan and Randall (1998)/Emori et al. (2001)	Y/N/N	CAPE/relative humidity
Same as above	MIROC3.2(medres) (MIROC-medres)	Spectral T42/L20 30 km	Pan and Randall (1998)/Emori et al. (2001)	Y/N/N	CAPE/relative humidity
MRI	MRI-CGCM2.3.2 (MRI)	Spectral T42/L30 0.4 mb	Pan and Randall (1998)	Y/N/N	CAPE
Canadian Centre for Climate Modeling and Analysis	CGCM3.1-T47 (CGCM)	Spectral T47*L32 1 mb	Zhang & McFarlane (1995)	Y/N/N	CAPE
MPI	ECHAM5/MPI-OM (MPI)	Spectral T63/L31 10 mb	Tiedtke (1989)/ Nordeng (1994)	Y/N/N	CAPE/moisture convergence
IPSL	IPSL-CM4 (IPSL)	Grid point 96/72/L19	Emanuel (1991)	Y/Y/N	CAPE
Météo-France/CNRM	CNRM-CM3 (CNRM)	Spectral T63/L45 0.05 mb	Bougeault (1985)	N/N/N	Kuo
CSIRO Atmospheric Research	CSIRO Mk3.0 (CSIRO)	Spectral T63/L18 4 mb	Gregory and Rowntree (1990)	Y/N/N	Cloud base buoyancy

* For downdrafts, SC means saturated convective downdrafts, UC means unsaturated convective downdrafts, and Meso means mesoscale downdrafts; indicated by yes (Y) or no (N).

runs]. The observed large-scale precipitation (Fig. 1a) pattern is one of intense precipitation over the Amazon basin, an eastern Pacific intertropical convergence zone (ITCZ), an Atlantic ITCZ, plus a band of enhanced precipitation that extends to the southeast from the maximum in the Amazon, known as the SACZ (e.g., Kodama 1992).

Most of the models underestimate precipitation over the Amazon basin. Only a few models produce magnitude close to that observed {i.e., the Model for Interdisciplinary Research on Climate 3.2, high-resolution version [MIROC3.2(hires)] and the Parallel Climate Model (PCM)}. The maximum is shifted to the east in three models [i.e., the Geophysical Fluid Dynamics Laboratory model version 2.0 (GFDL2.0), the Goddard Institute for Space Studies Atmosphere–Ocean Model (GISS-AOM), and the Goddard Institute for Space Studies Model E-R (GISS-ER)]. There are local maxima over the Andes Mountains in eight models {i.e., PCM, GISS-AOM, the Model for Interdisciplinary Research on Climate 3.2, medium-resolution version [MIROC3.2(medres)], MIROC3.2(hires), the Meteorological Research Institute Coupled General Circulation Model, version 2.3.2a (MRI CGCM), L'Institut Pierre-Simon Laplace (IPSL), Centre National de Recherches Météorologiques (CNRM)} that do not exist in GPCP. However, it is important to note that some other precipitation analyses for South America depict a precipitation maximum along the tropical Andes (e.g., Hoffman 1975). The eastern Pacific ITCZ is shifted south

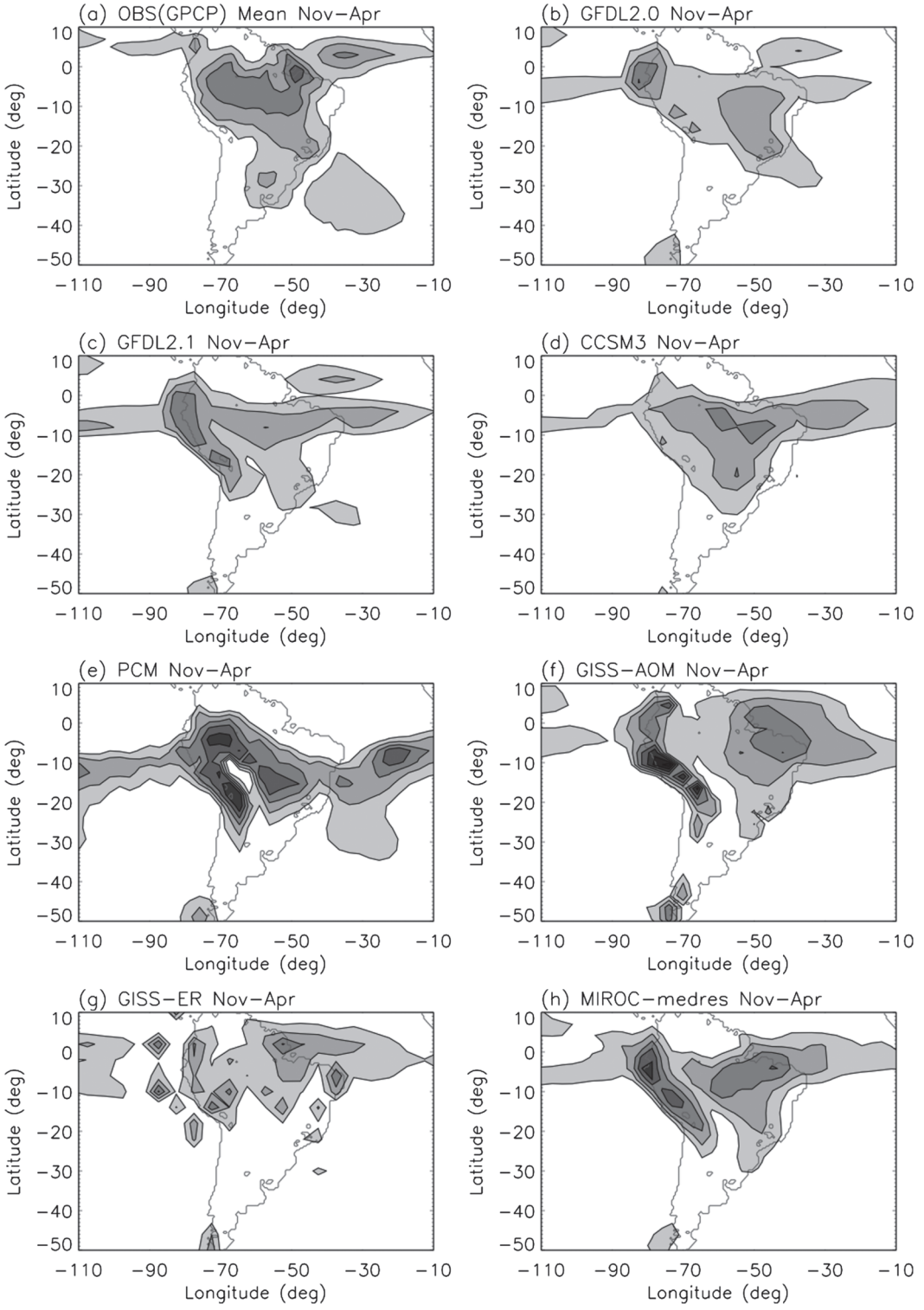

FIG. 1. Southern summer (November–April) seasonal mean precipitation for observation and 14 IPCC AR4 models. The first contour is 4 mm day^{-1} and the contour interval is 2 mm day^{-1}.

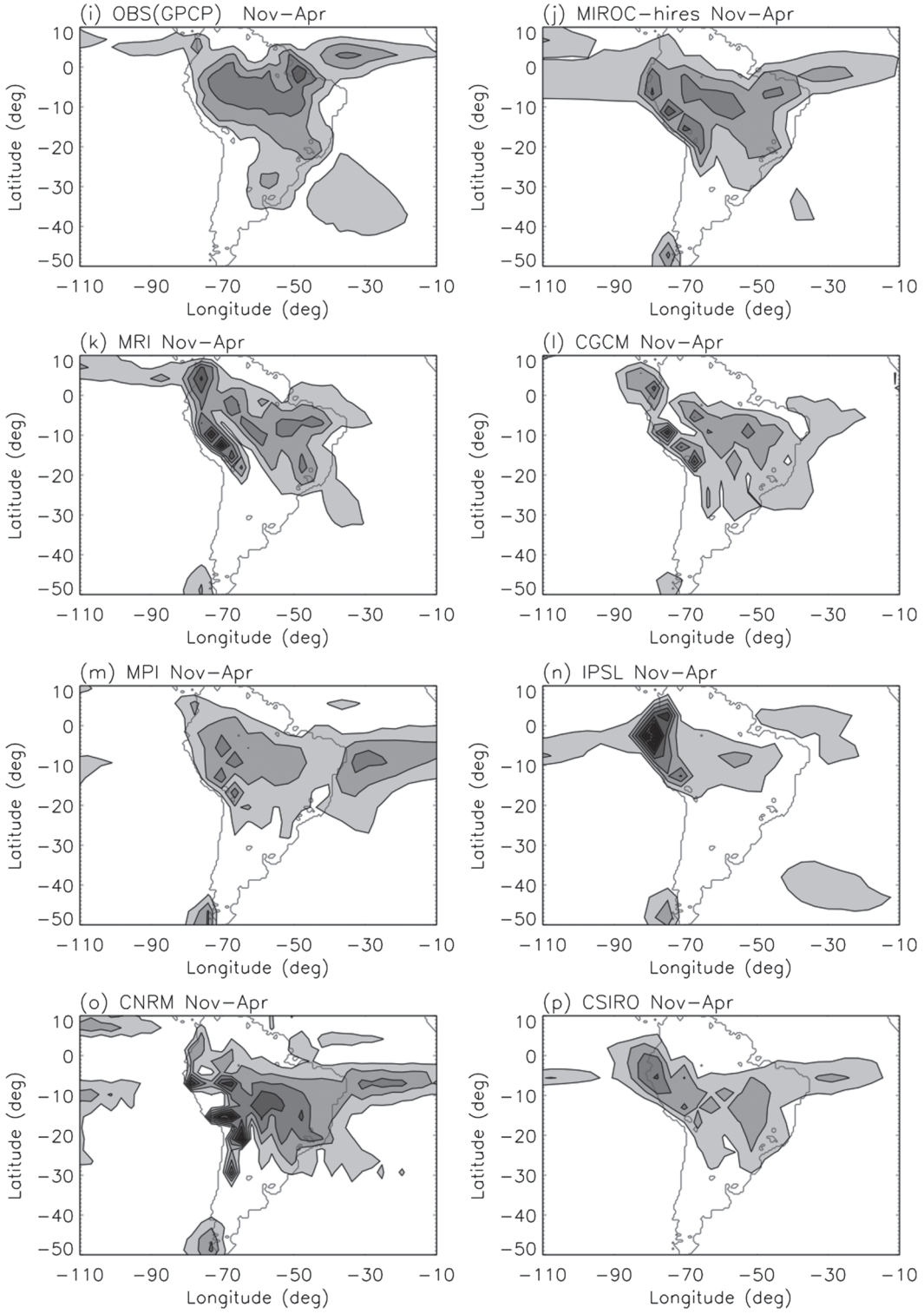

FIG. 1. (*Continued*)

of the equator in five models [i.e., the Community Climate System Model, version 3 (CCSM3), PCM, GISS-ER, IPSL, Commonwealth Scientific and Industrial Research Organisation (CSIRO)] and there is a double-ITCZ pattern in the eastern Pacific in six models [i.e., GFDL2.0, GFDL2.1, GISS-AOM, MIROC3.2(medres), MIROC3.2(hires), CNRM; see also Lin 2007]. The Atlantic ITCZ is too far south in almost all models, and two models (i.e., GFDL2.0 and GFDL2.1) show a double-ITCZ pattern in the tropical Atlantic. Finally, simulated precipitation in the SACZ is almost always too weak, and in the seven models that do contain an SACZ signature it is shifted northward with respect to observations [i.e., GFDL2.0, GFDL2.1, PCM, MIROC3.2(hires), MRI, the Max Planck Institute (MPI), and CNRM].

As will be shown shortly, the largest intraseasonal variability associated with summer precipitation over South America is concentrated in a meridional belt between 30° and 60°W (roughly the eastern continent and the western Atlantic Ocean). Therefore, we conduct a more quantitative evaluation of the seasonal mean precipitation averaged over these longitudes (Fig. 2). Observations reveal two local maxima: one at 2°S corresponding to the Amazon precipitation and Atlantic ITCZ, and a secondary peak at 30°S corresponding to the SACZ. Almost all of the models show only one maximum. In total 11 models have their maximum shifted southward compared to observed, to 10°S [i.e., GFDL2.0, CCSM3, GISS-AOM, MIROC3.2(hires), MRI, CGCM, MPI, IPSL, CSIRO] or 15°S (i.e., PCM and CNRM), which is associated with overly weak Amazon precipitation, and/or the southward shift of Amazon precipitation/Atlantic ITCZ in those models. All models underestimate the precipitation at 30°S, which is often associated with a too weak SACZ extension into the Atlantic. For the region between 10° and 25°S, 9 of the 14 models produce quite reasonable precipitation [i.e., GFDL2.0, CCSM3, GISS-AOM, MIROC3.2(medres), MIROC3.2(hires), MRI, CGCM, MPI, IPSL, CSIRO], while two models overestimate precipitation (i.e., PCM and CNRM) and three models underestimate it (i.e., GFDL2.1, GISS-ER, and IPSL).

b. *Total intraseasonal (10–90 day) variance*

Figure 3 shows the horizontal distribution of the standard deviation of total intraseasonal (10–90 day) precipitation anomaly during the November–April season. In observations (Fig. 3a), the intraseasonal variance does not completely follow that of seasonal mean precipitation (Fig. 1a), but is concentrated from approximately 10°N–40°S between 30° and 60°W. There are three local maxima: over the Amazon River mouth, over the Atlantic extension of the SACZ, and over southeast

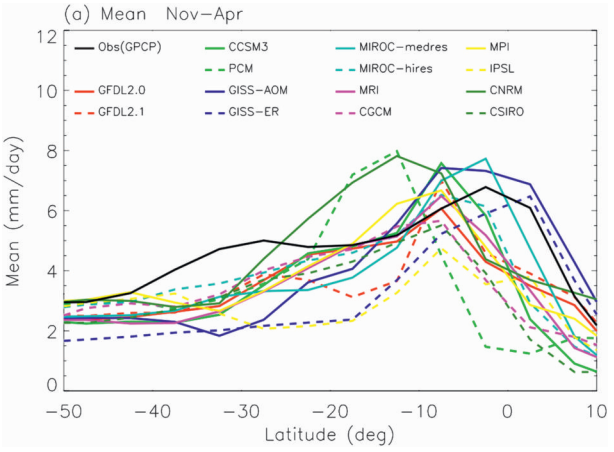

FIG. 2. Meridional profile of southern summer (November–April) seasonal mean precipitation averaged between 30° and 60°W for the observations and the 14 models.

Brazil/Uruguay. These are consistent with the results of Liebmann et al. (1999). The mismatch between the seasonal mean precipitation and total intraseasonal variance suggests that the intraseasonal variability is more than simply noise around the seasonal mean, but is caused by mechanisms that vary from those related to seasonal mean precipitation. Therefore, it is of interest as to whether if the models are able to reproduce this mismatch. The model variances show two characteristics. First, in 8 of the 14 models the distribution of intraseasonal variance does not completely follow that of the seasonal mean precipitation [i.e., GFDL2.0, GFDL2.1, MIROC3.2(hires), MRI, CGCM, MPI, IPSL, and CSIRO]. In three models the intraseasonal variance follows the mean precipitation [i.e., PCM, MIROC3.2(medres), and CNRM], and in three models the intraseasonal variance is too small (i.e., CCSM3, GISS-AOM, and GISS-ER). Second, the models tend to produce their maximum variance over their SACZ, but fail to produce the maxima over the Amazon River mouth or Uruguay.

To provide a more quantitative evaluation of the model simulations, Fig. 4 shows the meridional profile of total intraseasonal (10–90 day) variance of precipitation averaged between 30° and 60°W. The observed variance shows three peaks at 2°, 17°, and 32°S. All models underestimate the variance around 2° and 32°S. Only a few of the models produce any sort of a peak at all in those regions. For the region between 10° and 25°S, six models simulate nearly realistic or overly large variance [i.e., MIROC3.2(medres), MIROC3.2(hires), MPI, CNRM, CSIRO, and GFDL2.0]. The other eight models underestimate variance, although six of the eight display reasonable seasonal mean precipitation in this region (Fig. 2). Interestingly, the six models simulating nearly

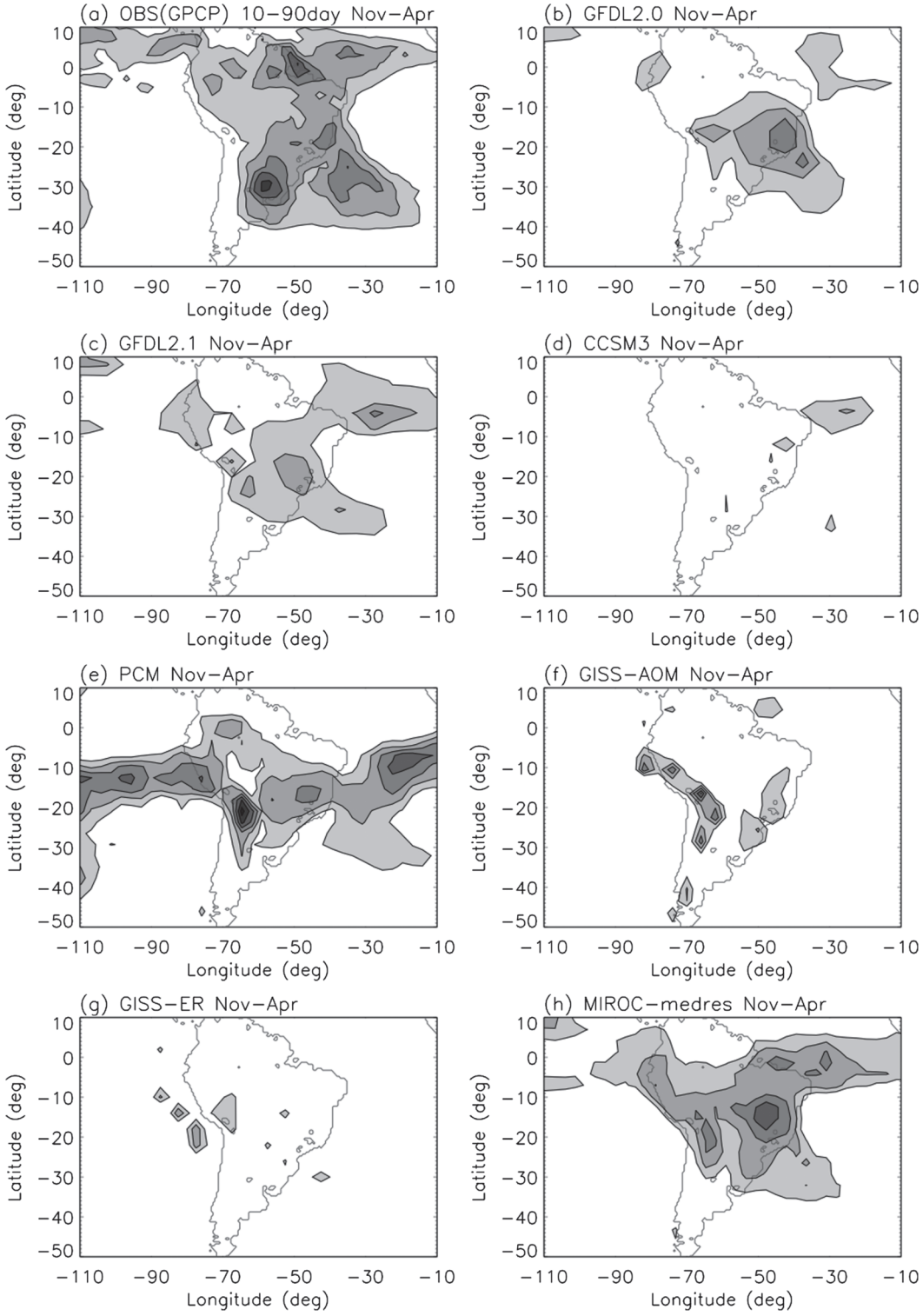

FIG. 3. Horizontal distribution of the standard deviation of total intraseasonal (10–90 day) precipitation anomaly during northern summer (November–April). The first contour is 3 mm day^{-1} and the contour interval is 1 mm day^{-1}.

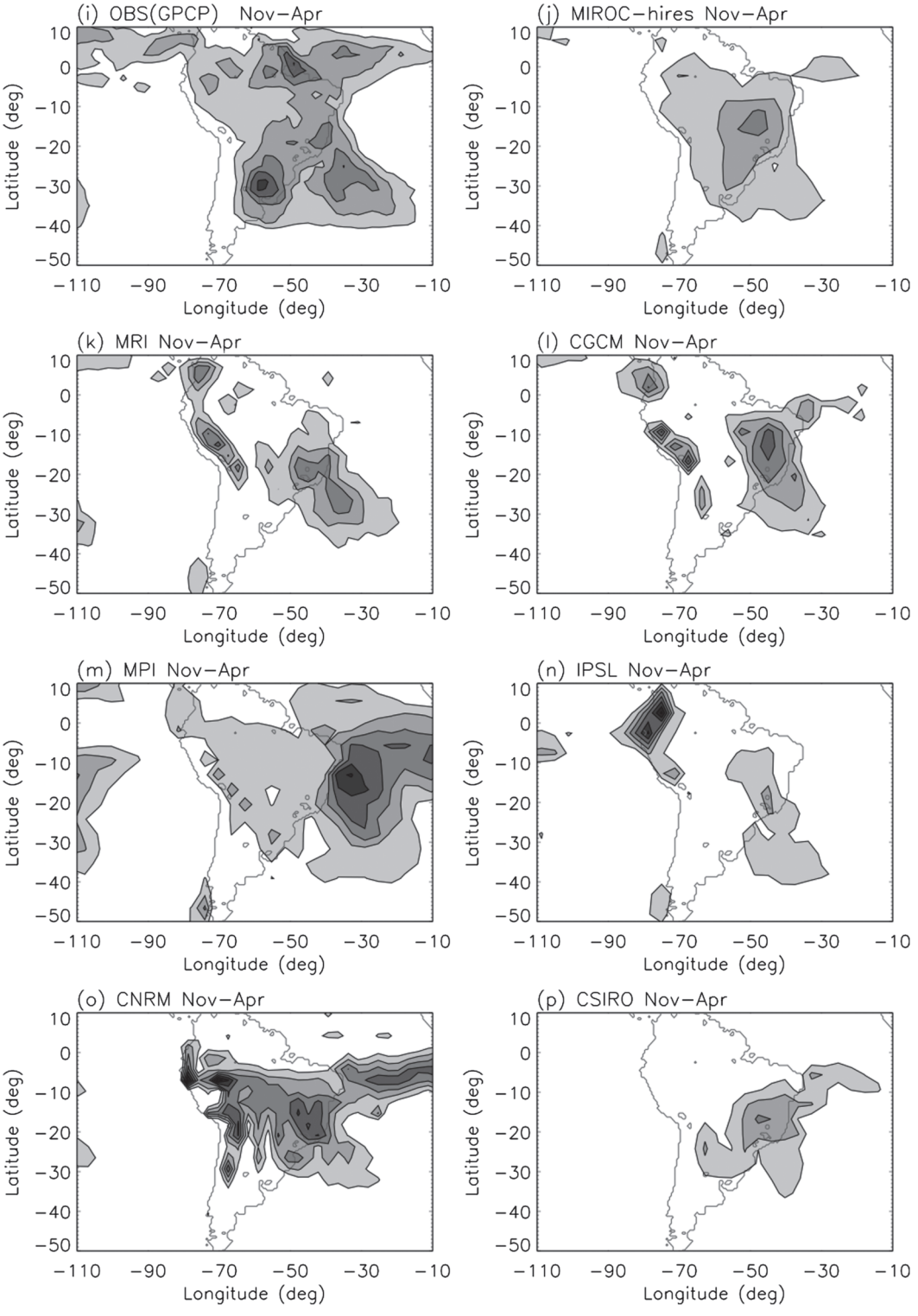

FIG. 3. (*Continued*)

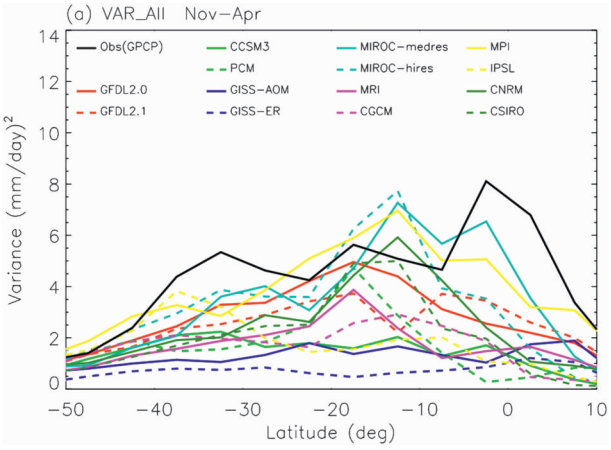

FIG. 4. Meridional profile of the total intraseasonal (10–90 day) variance of precipitation anomaly averaged between 30° and 60°W.

realistic or overly large variance are the same models that contain large variances for the convectively coupled equatorial waves (Lin et al. 2006). A common characteristic of these models is that there is some form of moisture trigger of their convection scheme, suggesting that a moisture trigger for deep convection may improve the simulation of intraseasonal variability associated with summer precipitation over South America.

c. *The dominant intraseasonal bands*

Figure 5 shows the wavelet spectrum of precipitation averaged between 30°–35°S, 50°–60°W (around Uruguay) for observations and the 14 IPCC models. The observed spectrum (Fig. 5a) demonstrates two dominant intraseasonal bands, a 30–60-day band (the so-called 40-day band) and a 20–30-day band (the so-called 22-day band). Most of the models capture both bands, although the model variances are generally smaller than the observed variances. The models also tend to produce fewer active episodes. Only two models (i.e., CGCM and CSIRO) produce frequent active episodes in both bands. It is important to note that many models have excessively large power between 60 and 100 days. This suggests that the summer precipitation in the models has larger persistence than is observed. Lin et al. (2006) found a similar problem associated with the tropical oceanic precipitation in the models, and hypothesized that it is caused by the erroneous representation of self-suppression processes in deep convection in the model's moisture physics.

d. *The 40-day band*

Next we focus on the 40-day band. Figure 6 shows the meridional profile of the 40-day band variance averaged between 30° and 60°W. The observed variance in the 40-day band is similar to the total intraseasonal variance in that there are peaks at 2°, 17°, and 32°S. At 40 days, however, the maximum at 17°S is larger than that at 32°S, while for the total intraseasonal variance (Fig. 4) the 17°S peak is relatively small, and is about the same as that at 32°S. All models underestimate the variance near 2° and 32°S. For the region between 10° and 25°S, the six models producing realistic or excessive total intraseasonal variance produce the 40-day band variance that is between the observed value and half the observed value, and the wavelet analysis (Fig. 5) suggests that their intraseasonal variance is concentrated more in the lower-frequency band. The other eight models produce the 40-day variance that is less than half of the observed value, although six of them display reasonable seasonal mean precipitation in this region (Fig. 2). Possible reasons of this will be discussed in section 4. It is important to note that although the models do not simulate the right intensity of variance, some are able to simulate the position of its peaks (e.g., GFDL2.0 and MPI).

Figure 7 shows the lag correlation of 40-day bandpass-filtered precipitation at 30°S, 55°W with the 40-day precipitation averaged from 50° to 60°W. Shading denotes the regions above the 95% confidence level. The observations (Fig. 7a), as expected, show a 40-day period oscillation at the latitude of the base grid point. Zonal anomalies of the opposite sign centered at about 15°S slightly lead those at the base grid point, resulting in a dipole pattern. Although the choice of base grid point makes the anomalies appear strongest at 30° and 15°S, the figure shows that the dipole actually propagates northward, with the opposite-signed anomalies that are evident at the latitude of the base grid point, but 20 days prior, moving northward to become the near-simultaneous antinode some 20° to the north. The observed northward propagation of the dipole is consistent with the results of Nogués-Paegle and Mo (1997) and Diaz and Aceituno (2003).

Only 2 of the 14 models capture both the northward propagation and the dipole [i.e., GISS-AOM and MIROC3.2(hires)]. One model captures only the northward propagation (MPI), while six models capture only the dipole [i.e., GFDL2.1, CCSM3, PCM, MIROC3.2(medres), MRI, and CGCM]. The other five models lack either of these features. It is important to note that the reason some models (e.g., GFDL2.0) do not show the dipole structure linking the subtropics to the tropics is because the tropical center in the model simulations is outside of the band 50°–60°W. For example, it will be shown (Fig. 11b) that such a dipolar structure is present in GFDL2.0, even though it is not evident in Fig. 7b.

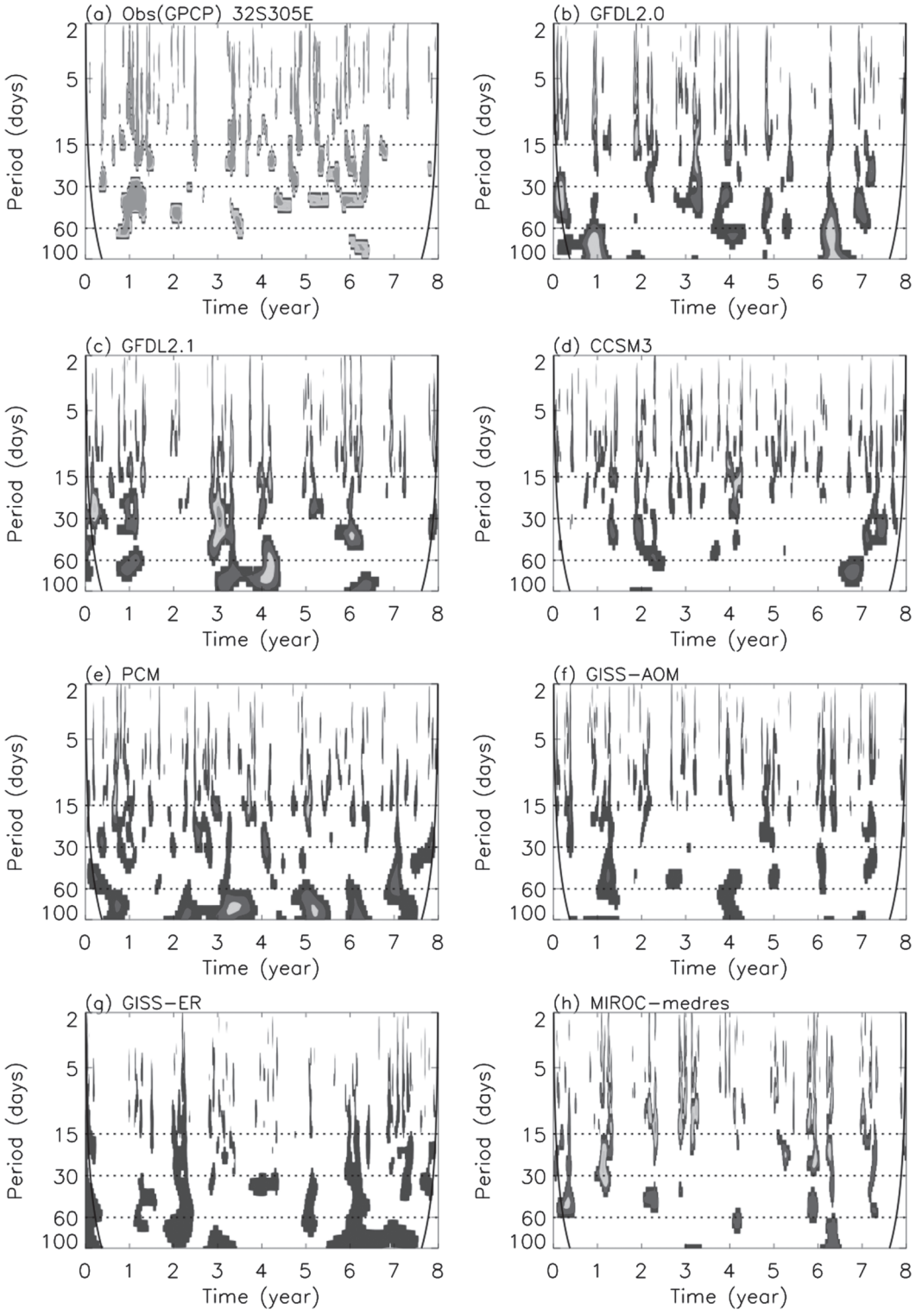

FIG. 5. Wavelet spectrum of precipitation averaged between 30°–35°S, 50°–60°W. Only spectral peaks above the 95% confidence level are plotted.

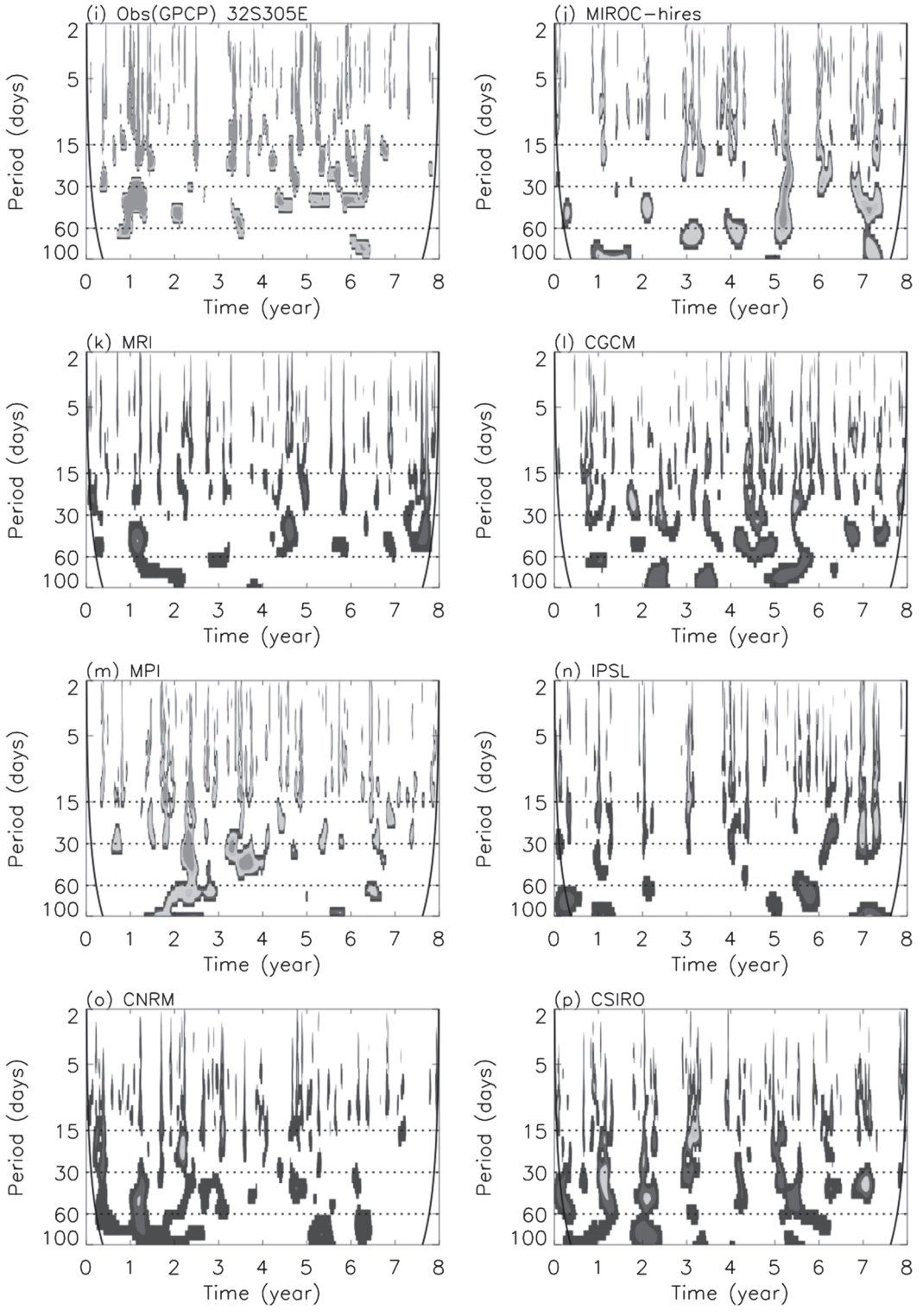

FIG. 5. (*Continued*)

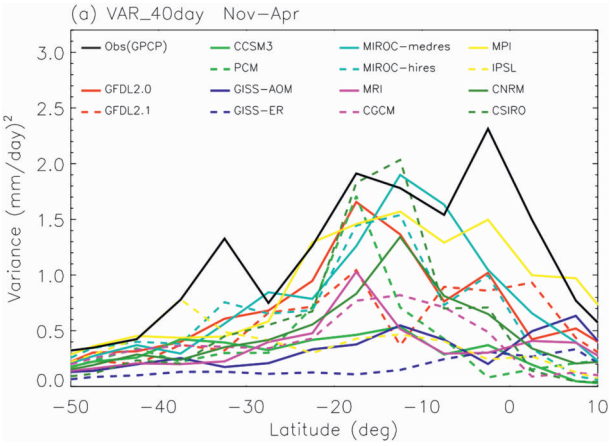

FIG. 6. As in Fig. 4, but for the variance of the 40-day band.

Next we examine the vertical structures of the models in the 40-day band. Figure 8 shows the lag correlation of temperature averaged between 20°–30°S and 50°–60°W versus the 40-day band precipitation anomaly at the same location for observation and the seven models with three-dimensional data available. Note that for four models the 3D data extends to only 200 mb. In observations, the 40-day band displays a deep warm core between the surface and 200 mb and a cold core above 250 mb during the convective phase. Six of the seven models show a significant warm temperature anomaly, but often with a large southward phase tilt with height.

There is also a significant bias in the geopotential height structure in many models (Fig. 9). The observed geopotential height displays a deep baroclinic structure, with a positive anomaly extending from the tropopause to 750 mb and a negative anomaly from 750 mb to the surface during the convective phase (Fig. 9a). Only one model (i.e., GFDL2.0) reproduces the deep baroclinic structure. In the other six models the negative anomaly extends too high into the middle/upper troposphere, indicating a more barotropic structure.

Figure 10 shows the vertical structure of divergence. The observed divergence displays a two-layer structure during the precipitating phase, with convergence from the surface to 450 mb, and divergence above 450 mb (Fig. 10a). All but one model (i.e., MPI) reproduce fairly well the two-layer structure, although in GFDL2.1 (Fig. 10c) the convergence layer is too deep, extending from the surface to 350 mb. Previous studies (e.g., Paegle et al. 2000) show that precipitation variability in the 30–60-day band observed at the region around 30°S, 55°W is associated with the activity of Rossby wave trains propagating into the region from the South Pacific. Therefore, it seems that biases associated with temperature, geopotential height, and divergence are related to modeling deficiencies in reproducing the features associated with the Rossby wave trains.

Next we look at the teleconnection pattern associated with the 40-day band. Figure 11 shows the linear correlation of the 40-day band precipitation anomaly versus itself averaged between 25°–35°S and 30°–60°W. In observations (Fig. 11a), there is a three-cell pattern around South America with a positive precipitation anomaly over Uruguay and negative anomalies over the SACZ and the South Pacific around 50°S, 280°E, which are all statistically significant above the 95% confidence level. This three-cell pattern has been found in previous observational studies using OLR (Carvalho et al. 2004, see their Fig. 8c) and upper-air geopotential height, streamfunction, and winds (Liebmann et al. 1999, 2004; Diaz and Aceituno 2003; Carvalho et al. 2004). At the same time, there is a dipole over the tropical Pacific with a negative anomaly over the central Pacific and positive anomaly over the Maritime Continent/western Pacific. These are consistent with the results of Paegle et al. (2000, see their Fig. 6d), and they demonstrated that the dipole over tropical Pacific is associated with the MJO. There is also a positive anomaly over south central Pacific around 20°S, 200°E with a SPCZ developed farther east of its climatological position, which is consistent with previous work (e.g., Nogués-Paegle and Mo 1997). In total, 10 of the 14 models simulate to some extent the three-cell pattern around the South America [i.e., GFDL2.0, GFDL2.1, GISS-AOM, MIROC3.2(medres), MRI, CGCM, MPI, IPSL, CNRM, and CSIRO]. However, only one model (i.e., GFDL2.0) simulates the MJO dipole over the tropical Pacific. Six models [i.e., GFDL2.1, PCM, GISS-ER, MIROC3.2(hires), CGCM, MPI, and IPSL] produce statistically a significant positive anomaly in the south-central Pacific around 20°S, 200°E.

To summarize, all models substantially underestimate the 40-day band variance over north Brazil and Uruguay, while about half of the models simulate nearly realistic variance over the SACZ. In total, 10 of the 14 models simulate to some extent the three-cell pattern around the South America, with 6 models reproducing its teleconnection with precipitation in the south-central Pacific. However, only one model simulates the teleconnection with the MJO in equatorial Pacific, and only three models capture its northward propagation from 50° to 32°S. Of the seven models with three-dimensional data available, only one reproduces well the deep baroclinic vertical structure of the 40-day band.

e. The 22-day band

Figure 12 shows the meridional profile of the 22-day band precipitation variance averaged between 30° and

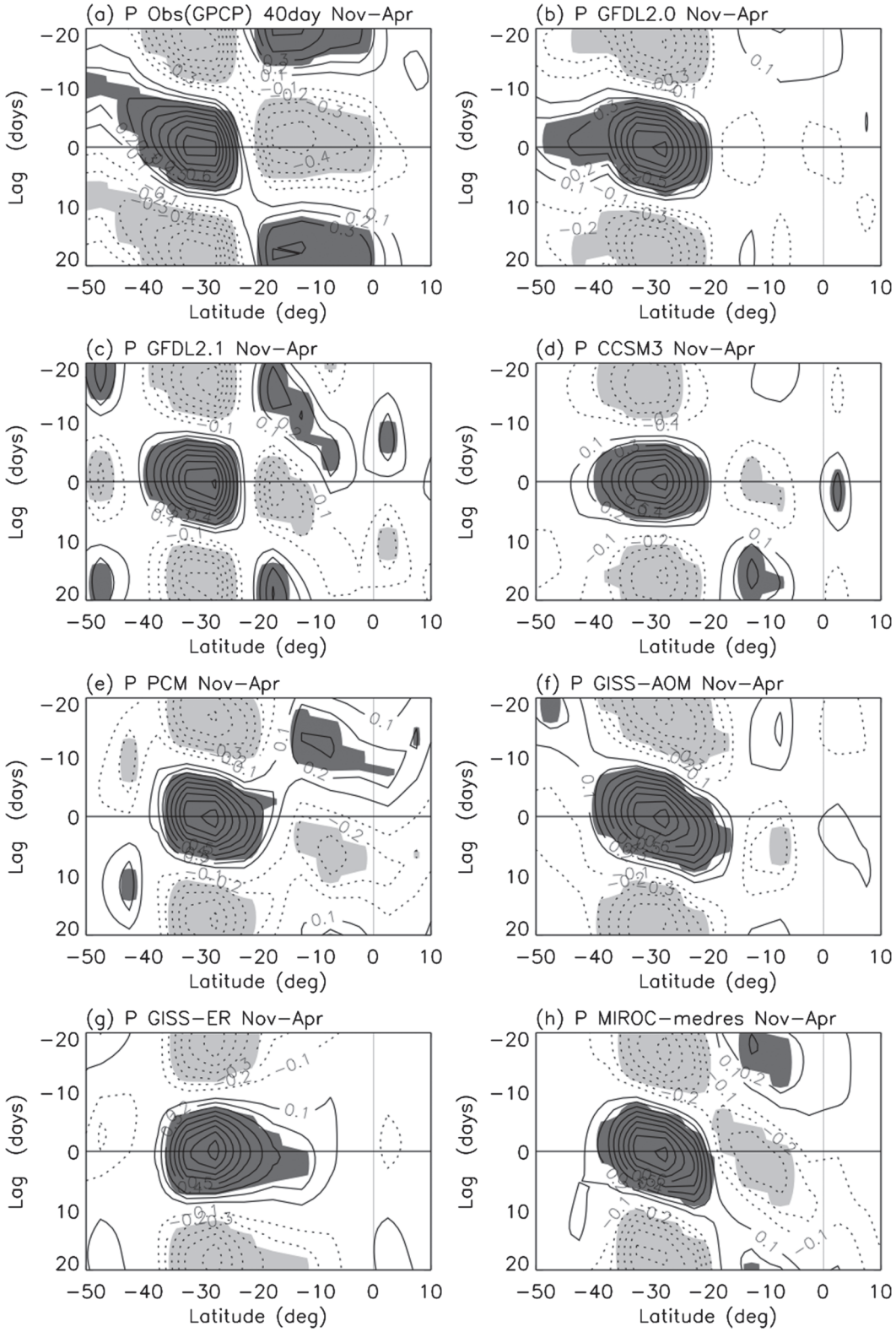

FIG. 7. Lag correlation of the 40-day band precipitation anomaly averaged between 50° and 60°W with respect to itself at 30°S, 55°W. Shading denotes the regions where the lag correlation is above the 95% confidence level.

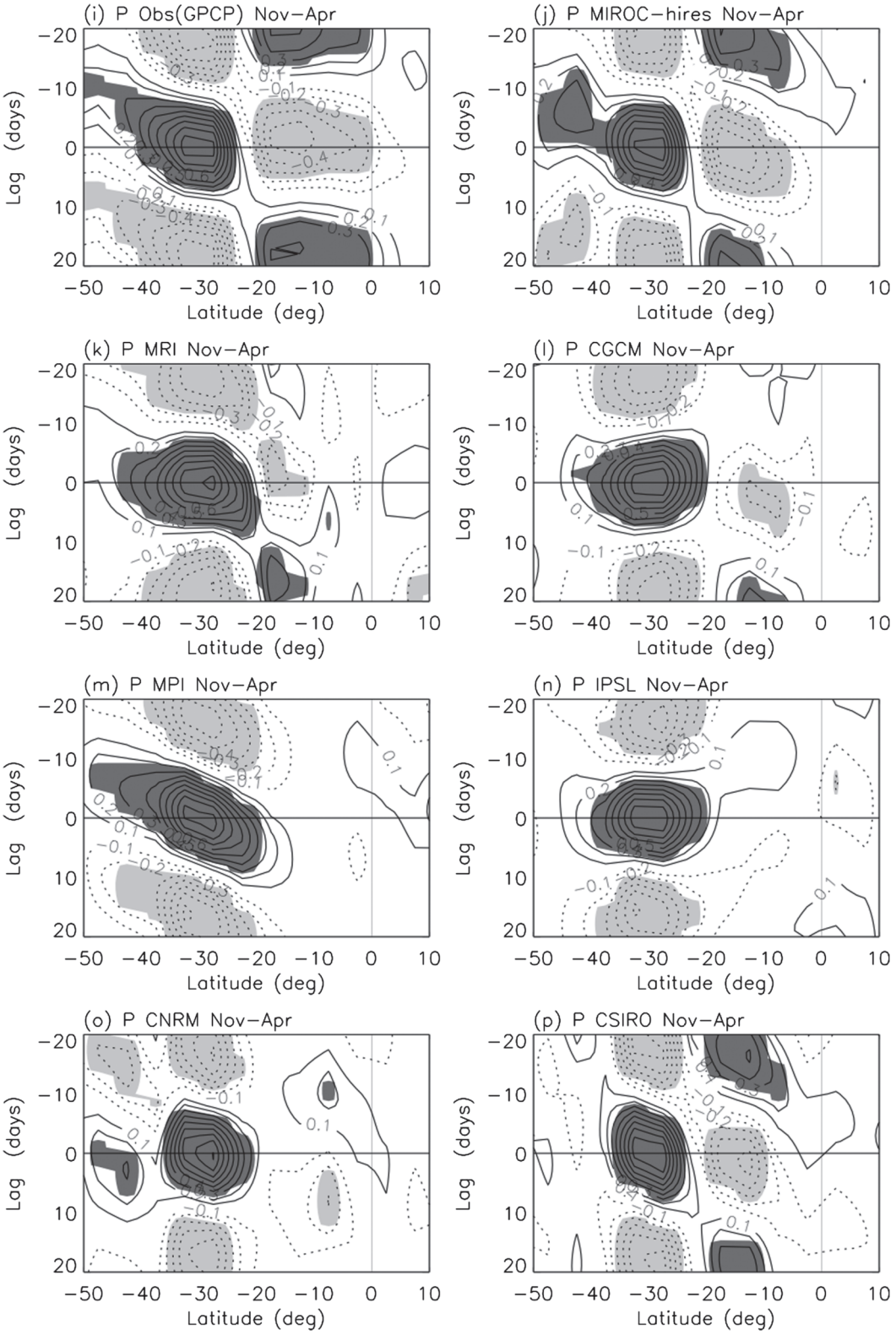

FIG. 7. (*Continued*)

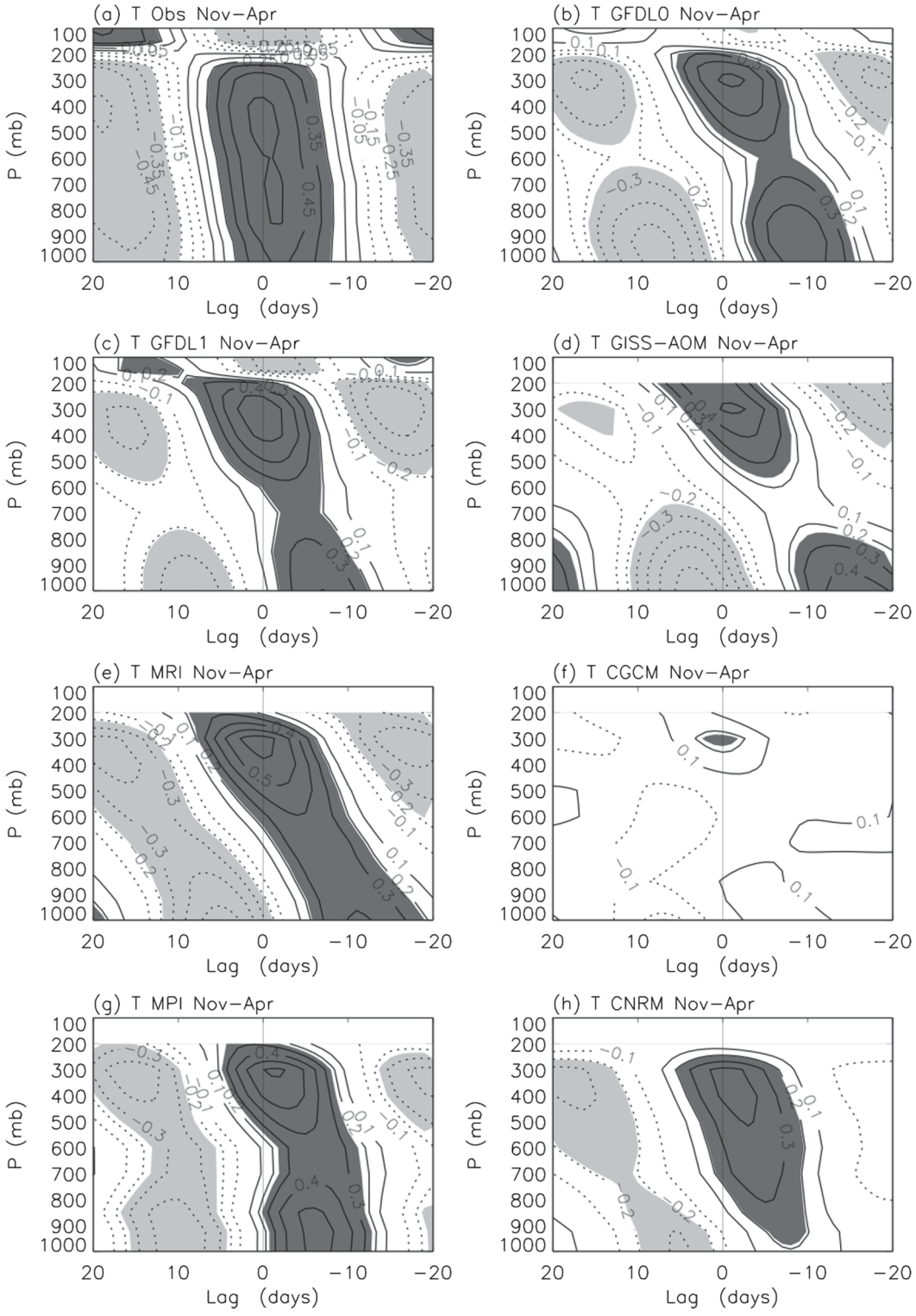

FIG. 8. Lag correlation of temperature averaged between 20°–30°S and 50°–60°W vs the 40-day band precipitation anomaly at the same location for observation (NCEP–NCAR reanalysis) and the seven models. Shading denotes the area where correlation is above the 95% confidence level, with dark (light) shading for positive (negative) correlation.

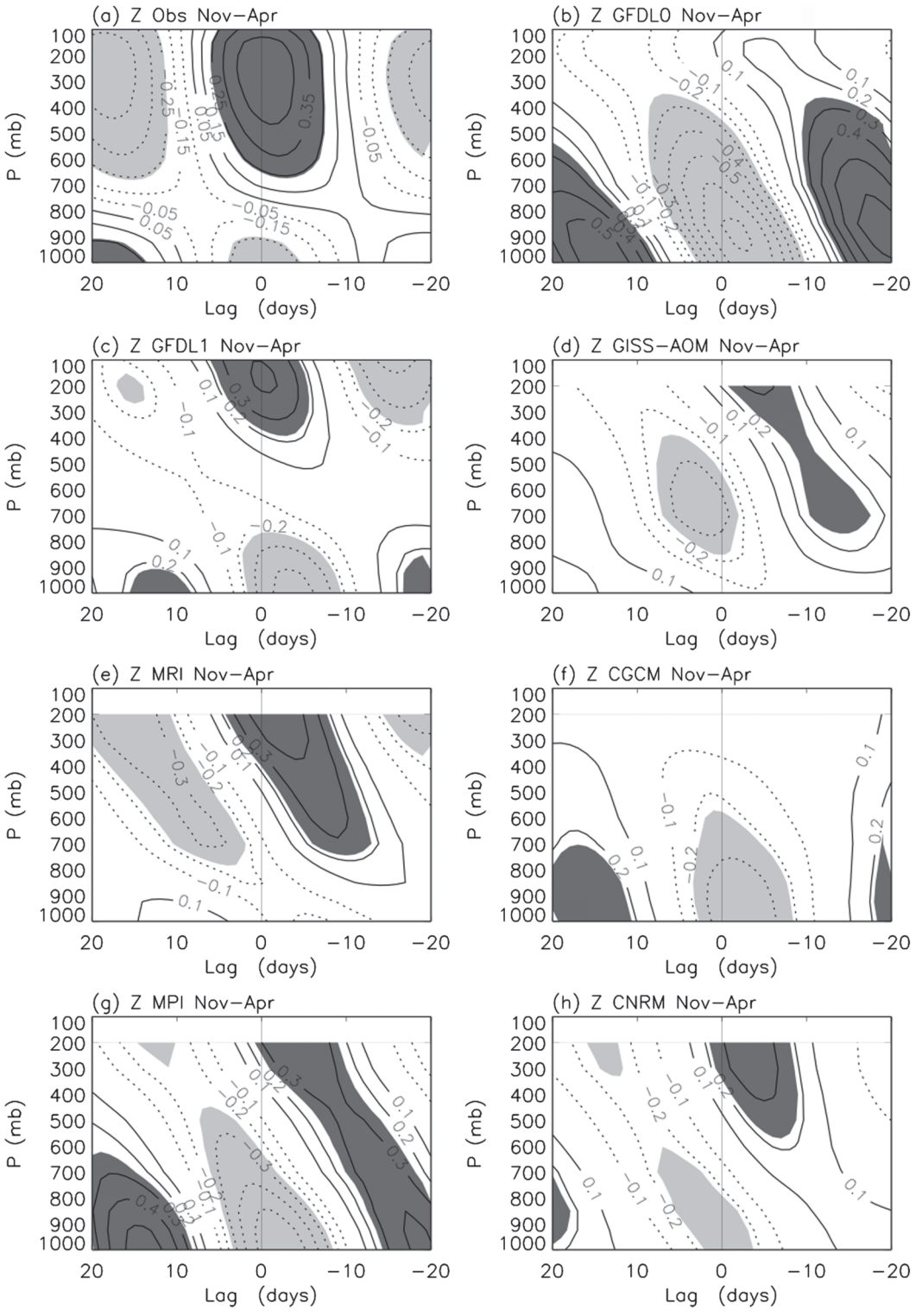

FIG. 9. As in Fig. 8, but for geopotential height.

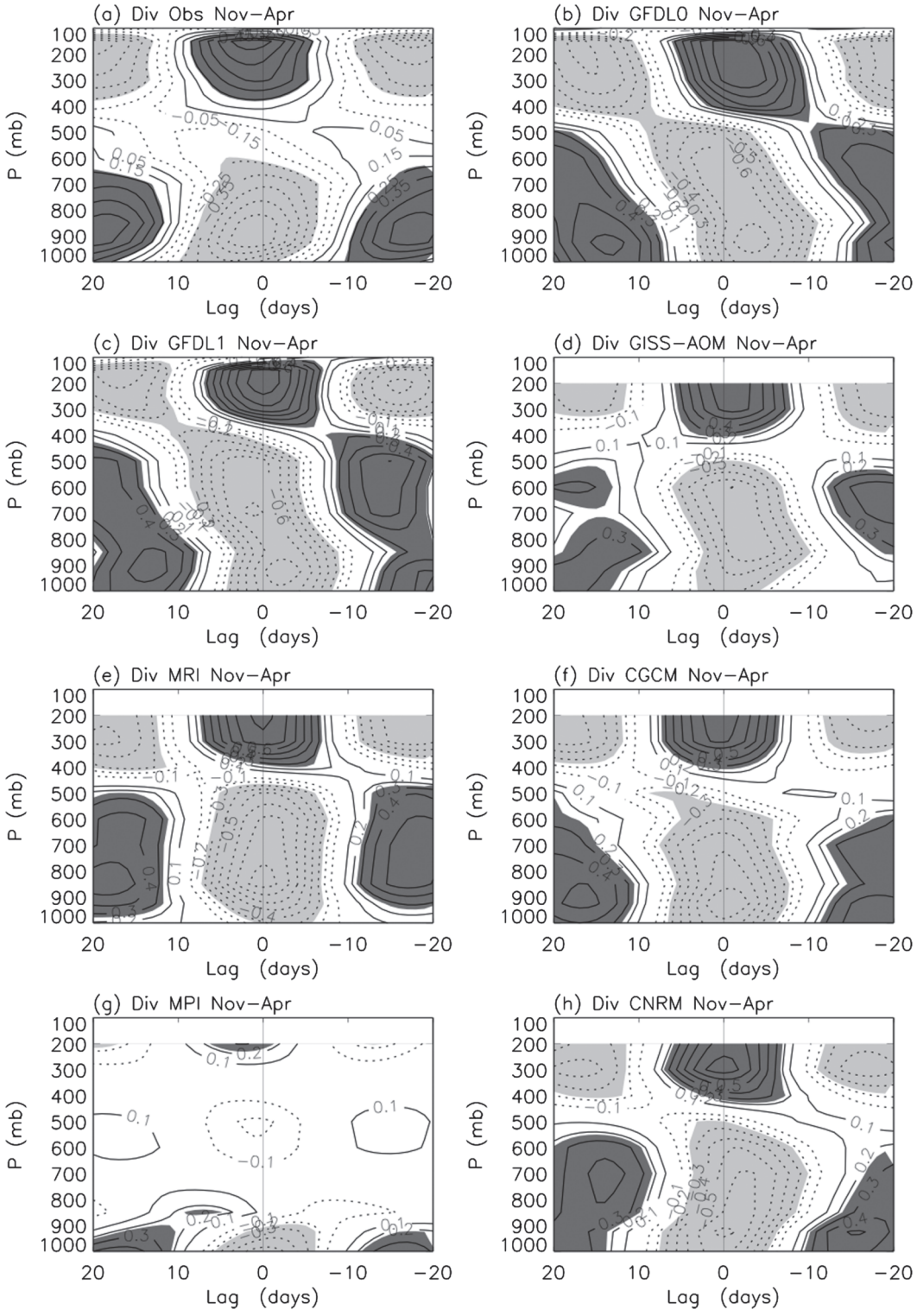

FIG. 10. As in Fig. 8, but for divergence.

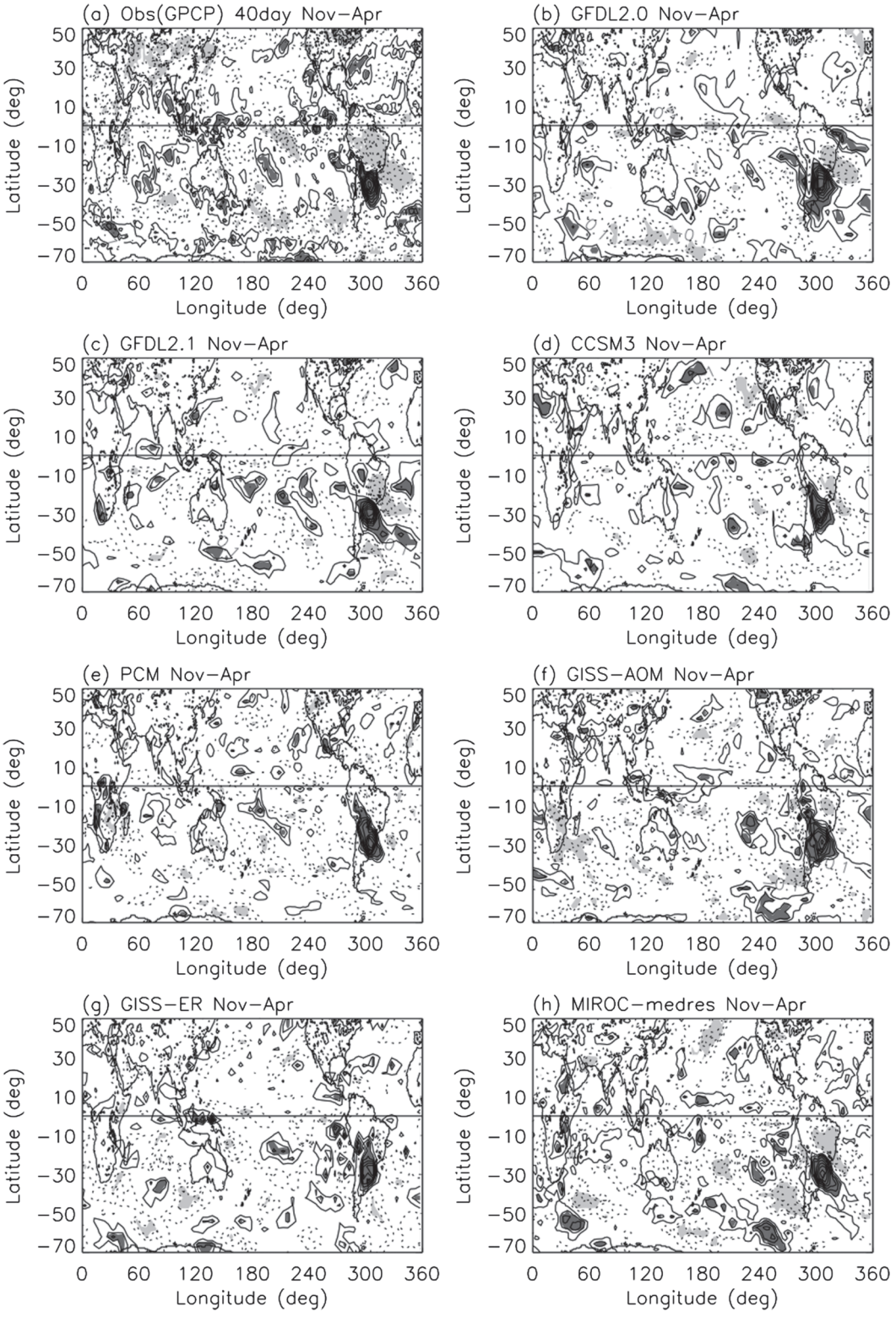

FIG. 11. Linear correlation of the 40-day band precipitation anomaly vs itself averaged between 25°–35°S and 50°–60°W. Shading denotes the area where correlation is above the 95% confidence level, with dark (light) shading for positive (negative) correlation.

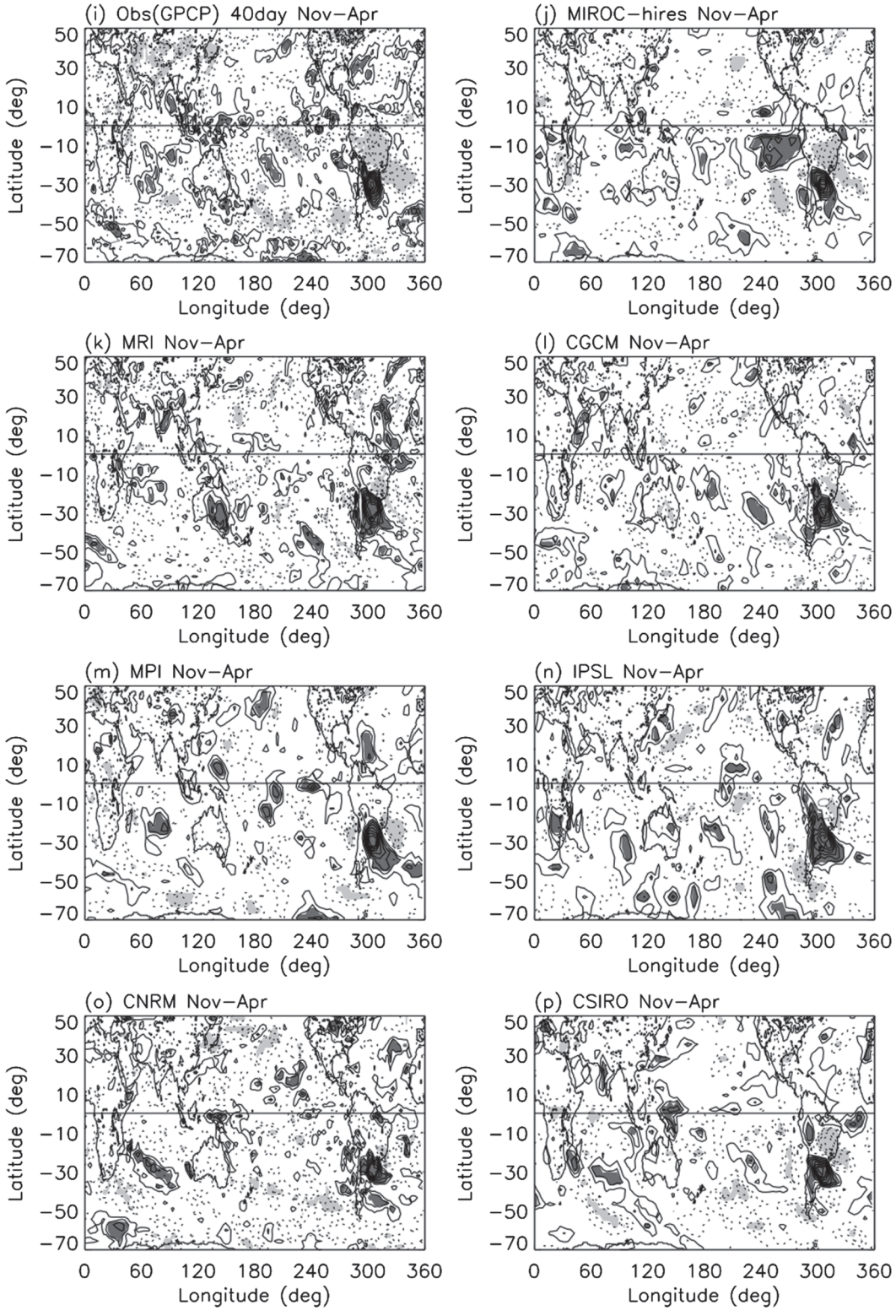

FIG. 11. (*Continued*)

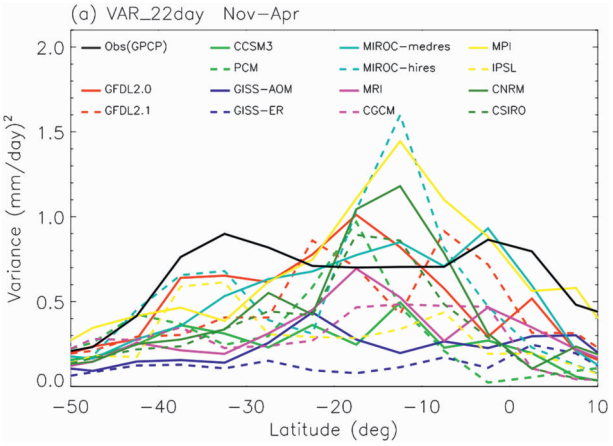

FIG. 12. As in Fig. 4, but for the variance of the 22-day band.

60°W. The observed profile of the 22-day band variance is different from those of the total intraseasonal (10–90 day) variance (Fig. 4) and the 40-day band variance (Fig. 6), both of which display three local maxima with the primary maximum at 2°S. The 22-day band, on the other hand, shows only two maxima at 2°S and 32°S with the later having slightly larger magnitude. In total, 12 of the 14 models underestimate the variance around 2°S, and all models underestimate the variance around 32°S. Between 10° and 25°S, six models simulate realistic or overly large variance [i.e., MIROC3.2(hires), MPI, CNRM, GFDL2.0, MIROC3.2(medres), and CSIRO]. Again, these are those models producing large variances for the convectively coupled equatorial waves (Lin et al. 2006).

Figure 13 shows the lag-correlation of the 22-day band precipitation anomaly averaged between 30° and 60°W with respect to the 22-day band precipitation anomaly at 30°S, 55°W. In observations (Fig. 13a), the 22-day band propagates northward from 40°S (precipitation activity over southeastern subtropical South America) to the equator (Atlantic ITCZ), which is consistent with the results of Paegle et al. (2000, see their Fig. 10f). In total, 6 of the 14 models simulate coherent northward propagation [i.e., GFDL2.1, GISS-AOM, MIROC3.2(medres), MIROC3.2(hires), MPI, and CSIRO], but the propagation often stops at 10°S, which is consistent with the southward shift of the Atlantic ITCZ in the models (Figs. 1 and 2). Seven models produce standing oscillation (i.e., GFDL2.0, CCSM3, PCM, MRI, CGCM, IPSL, and CNRM), and one model displays different propagation direction in different regions (i.e., GISS-ER).

4. Summary and discussion

This study evaluates the intraseasonal variability associated with the summer precipitation over South America in 14 IPCC AR4 coupled GCMs. The results show that in the southern summer (November–April), most of the models underestimate seasonal mean precipitation over central-east Brazil, northeast Brazil, and the SACZ. Most models produce and Atlantic SACZ to the south of that observed. Most of the models capture both the 40- and 22-day bands around Uruguay, but with fewer active episodes than observed. The models also tend to underestimate the total intraseasonal (10–90 day) variance, the 40-day band variance, and the 22-day band variance. In the 40-day band, 10 of the 14 models simulate to some extent the three-cell pattern around South America, and six models reproduce its teleconnection with precipitation in the south-central Pacific, but only one model simulates the teleconnection with the MJO in equatorial Pacific, and only three capture its northward propagation from 50° to 32°S. Of the seven models with three-dimensional data available, only one reproduces well the deep baroclinic vertical structure of the 40-day band. For the 22-day band, only 6 of the 14 models capture its northward propagation from the SACZ to the Atlantic ITCZ.

Factors hypothesized to be important for simulating subseasonal variability include air–sea interaction, land–atmosphere interaction, model resolution, and model physics. Regarding air–sea interaction, all models analyzed in this study are coupled GCMs, but they still have significant difficulties in simulating the subseasonal variability. However, previous studies have shown that the effects of coupling depend strongly on the background state (e.g., Inness et al. 2003; Turner et al. 2005). Without detailed experimentation using coupled and uncoupled versions of the same model *with similar mean states*, few firm conclusions can be drawn. Moreover, since most coupled models are only exchanging air–sea or air–land fluxes once every 24 h, more frequent coupling may be necessary.

Land–atmosphere interaction may also play an important role in simulating the intraseasonal variability in the monsoon regions (e.g., Webster 1983). In an observational study, evidence was found that the 40-day band could be locally excited by interaction with the land surface states and fluxes in the Amazon rain forest. Future studies are needed to assess how well the IPCC models simulate the land–atmosphere interaction over the Amazon rain forest.

Regarding model resolution, we have only one pair of similar atmospheric models but with different resolution: MIROC3.2(hires; T106) versus MIROC3.2(medres; T42). Higher model resolution is associated with weaker variance of the 40-day band (Fig. 6), but stronger variances of the 22-day band (Fig. 12). It improves the propagation of the 40-day band (Fig. 7) but not the 22-day band (Fig. 13).

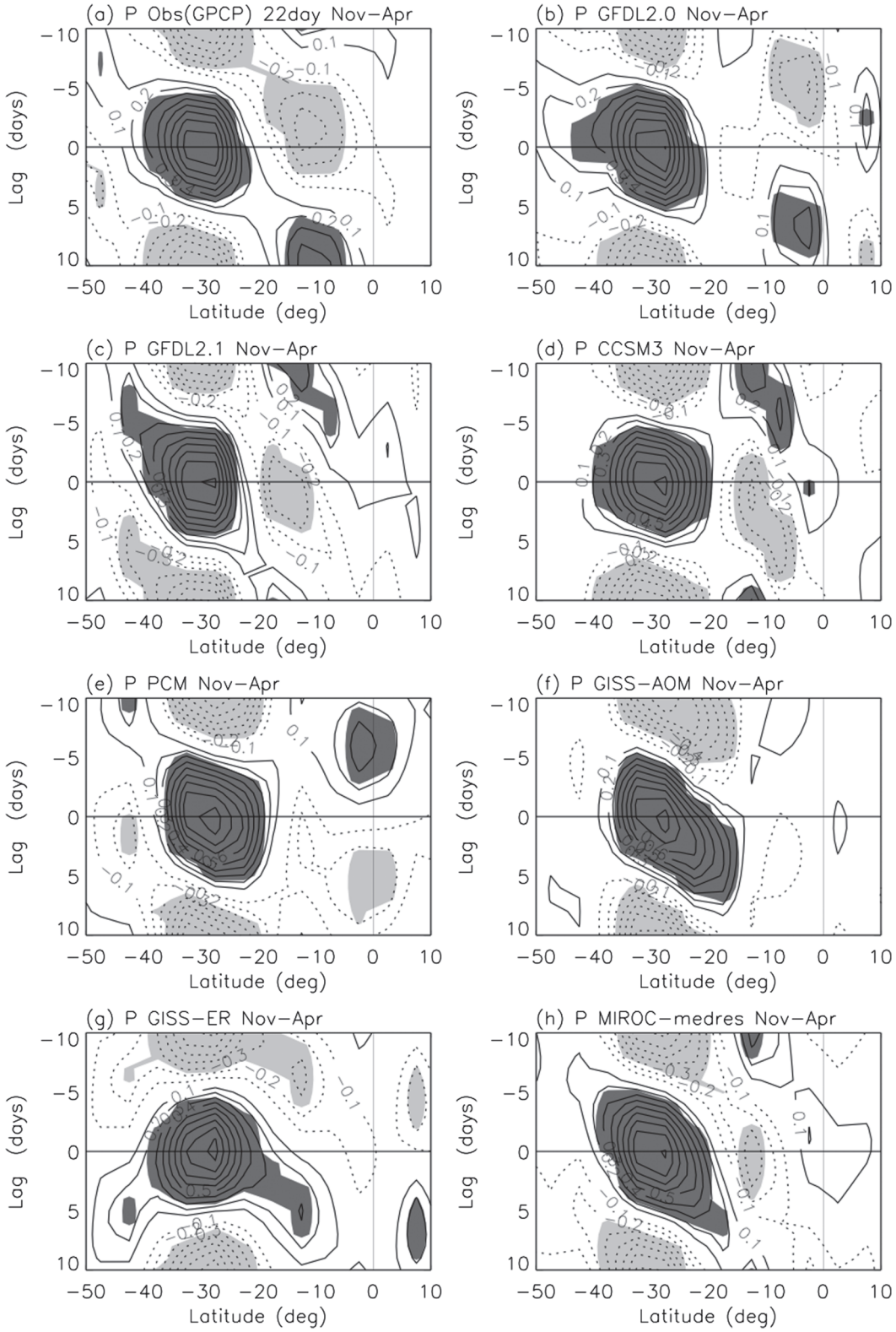

FIG. 13. Lag correlation of the 22-day band precipitation anomaly averaged between 50° and 60°W with respect to itself at 30°S, 55°W. Shading denotes the regions where lag correlation is above the 95% confidence level.

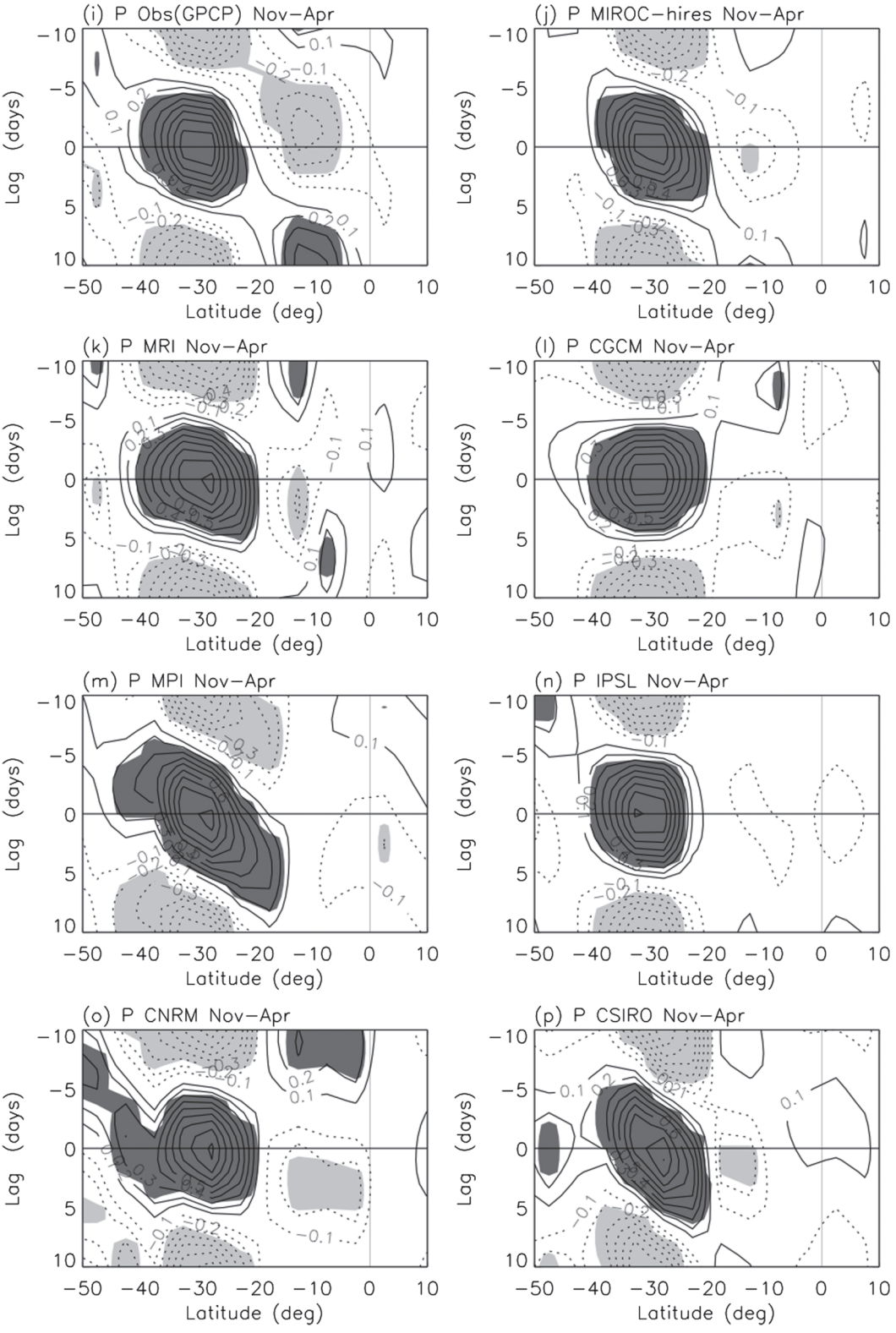

FIG. 13. (*Continued*)

However, these results may be model dependent, since the resolution dependence is often related to the specific characteristics of model physics. Moreover, model resolution also affects the representation of topography, such as the Andes Mountains, which may alter the Rossby wave trains that enter into South America from the South Pacific. Since all of our models are in a relatively low resolution (Table 1), with the highest resolution (T106) being about 125 km, the poor representation of the Andes Mountains may contribute to the model limitations in correctly representing subseasonal variability in South America.

Regarding model physics, an interesting finding of this study is that the six models simulating large total intraseasonal, 40- and 22-day band variances [i.e., MIROC3.2(hires), MPI, CNRM, GFDL2.0, MIROC3.2(medres), and CSIRO] are just the models producing large variances for the convectively coupled equatorial waves in the tropics (Lin et al. 2006). A common characteristic of these models is that there is some form of moisture trigger associated with their convection scheme. We have conducted a series of GCM sensitivity experiments to test the effects of moisture trigger on the simulated intraseasonal variability associated with summer precipitation over South America in the Seoul National University GCM. Three different convection schemes are used including the simplified Arakawa–Schubert (SAS) scheme, the Kuo (1974) scheme, and the moist convective adjustment (MCA) scheme, and a moisture convective trigger with variable strength is added to each scheme. The results show that adding a moisture trigger significantly enhance the variances of both the 40- and 22-day bands. The results will be reported in a separate study.

Acknowledgments. Gary Russell kindly provided a detailed description of the GISS-AOM model. We acknowledge the international modeling groups for providing their data for analysis, the Program for Climate Model Diagnosis and Intercomparison (PCMDI) for collecting and archiving the model data, the JSC/CLIVAR Working Group on Coupled Modeling (WGCM) and their Coupled Model Intercomparison Project (CMIP) and Climate Simulation Panel for organizing the model data analysis activity, and the IPCC WG1 TSU for technical support. The IPCC Data Archive at Lawrence Livermore National Laboratory is supported by the Office of Science, U.S. Department of Energy. J. L. Lin was supported by NASA Modeling, Analysis and Prediction (MAP) Program and NSF Grant ATM-0745872. T. Shinoda was supported by NSF Grants OCE-0453046 and ATM-0745897, an NOAA CPO/CVP Grant, and the 6.1 project Global Remote Littoral Forcing via Deep Water Pathways sponsored by the Office of Naval Research (ONR) under Program Element 601153N. The authors thank the three anonymous reviewers for their insightful comments that significantly improved the manuscript.

REFERENCES

Bougeault, P., 1985: A simple parameterization of the large-scale effects of cumulus convection. *Mon. Wea. Rev.,* **113,** 2108–2121.

Carvalho, L. M. V., C. Jones, and B. Liebmann, 2004: The South Atlantic convergence zone: Intensity, form, persistence, and relationships with intraseasonal to interannual activity and extreme rainfall. *J. Climate,* **17,** 88–108.

Del Genio, A. D., and M.-S. Yao, 1993: Efficient cumulus parameterization for long-term climate studies: The GISS scheme. *The Representation of Cumulus Convection in Numerical Models, Meteor. Monogr.,* No. 46, Amer. Meteor. Soc., 181–184.

Diaz, A., and P. Aceituno, 2003: Atmospheric circulation anomalies during episodes of enhanced and reduced cloudiness over Uruguay. *J. Climate,* **16,** 3171–3185.

Duchan, C. E., 1979: Lanczos filtering in one and two dimensions. *J. Appl. Meteor.,* **18,** 1016–1022.

Emanuel, K. A., 1991: A scheme for representing cumulus convection in large-scale models. *J. Atmos. Sci.,* **48,** 2313–2329.

Emori, S., T. Nozawa, A. Numaguti, and I. Uno, 2001: Importance of cumulus parameterization for precipitation simulation over East Asia in June. *J. Meteor. Soc. Japan,* **79,** 939–947.

Gregory, D., and P. R. Rowntree, 1990: A mass flux convection scheme with representation of cloud ensemble characteristics and stability-dependent closure. *Mon. Wea. Rev.,* **118,** 1483–1506.

Hoffman, J., 1975: Maps of mean temperature and precipitation. *Climatic Atlas of South America,* Vol. 1, WMO, 1–28.

Horel, J. D., A. N. Hahmann, and J. E. Geisler, 1989: An investigation of the annual cycle of convective activity over the tropical Americas. *J. Climate,* **2,** 1388–1403.

Huffman, G. J., R. F. Adler, M. M. Morrissey, S. Curtis, R. Joyce, B. McGavock, and J. Susskind, 2001: Global precipitation at one-degree daily resolution from multisatellite observations. *J. Hydrometeor.,* **2,** 36–50.

Inness, P. M., J. M. Slingo, E. Guilyardi, and J. Cole, 2003: Simulation of the Madden–Julian Oscillation in a coupled general circulation model. Part II: The role of the basic state. *J. Climate,* **16,** 365–382.

Jones, C., and L. M. Carvalho, 2002: Active and break phases in the South American monsoon system. *J. Climate,* **15,** 905–914.

Kalnay, E., and Coauthors, 1996: The NCEP/NCAR 40-Year Reanalysis Project. *Bull. Amer. Meteor. Soc.,* **77,** 437–471.

Kodama, Y. M., 1992: Large-scale common features of subtropical precipitation zones (the Baiu frontal zone, the SPCZ, and the SACZ). Part I: Characteristics of subtropical frontal zones. *J. Meteor. Soc. Japan,* **70,** 813–835.

Kousky, V. E., 1988: Pentad outgoing longwave radiation climatology for the South American sector. *Rev. Bras. Meteor.,* **3,** 217–231.

Kuo, H. L., 1974: Further studies of the parameterization of the influence of cumulus convection on large-scale flow. *J. Atmos. Sci.,* **31,** 1232–1240.

Lenters, J. D., and K. H. Cook, 1995: Simulation and diagnosis of the regional summertime precipitation climatology of South America. *J. Climate,* **8,** 2988–3005.

Liebmann, B., G. N. Kiladis, J. A. Marengo, T. Ambrizzi, and J. D. Glick, 1999: Submonthly convective variability over South America and the South Atlantic convergence zone. *J. Climate,* **12,** 1877–1891.

——, ——, C. S. Vera, and A. C. Saulo, 2004: Subseasonal variations of rainfall in South America in the vicinity of the low level jet east of the Andes and comparison to those in the South Atlantic convergence zone. *J. Climate,* **17,** 3829–3842.

Lin, J. L., 2007: The double-ITCZ problem in IPCC AR4 coupled GCMs: Ocean–atmosphere feedback analysis. *J. Climate,* **20,** 4497–4525.

——, and Coauthors, 2006: Tropical intraseasonal variability in 14 IPCC AR4 climate models. Part I: Convective signals. *J. Climate,* **19,** 2665–2690.

——, M.-I. Lee, D. Kim, I.-S. Kang, and D. M. W. Frierson, 2008: The impacts of convective parameterization and moisture triggering on AGCM-simulated convectively coupled equatorial waves. *J. Climate,* **21,** 883–909.

Mak, M., 1995: Orthogonal wavelet analysis: Interannual variability in the sea surface temperature. *Bull. Amer. Meteor. Soc.,* **76,** 2179–2186.

Mapes, B. E., and J. Lin, 2005: Doppler radar observations of mesoscale wind divergence in regions of tropical convection. *Mon. Wea. Rev.,* **133,** 1808–1824.

Meehl, G. A., C. Covey, T. Delworth, M. Latif, B. McAvaney, J. F. B. Mitchell, R. J. Stouffer, and K. E. Taylor, 2007: The WCRP CMIP3 multimodel dataset: A new era in climate change research. *Bull. Amer. Meteor. Soc.,* **88,** 1383–1394.

Misra, V., 2005: Simulation of the intraseasonal variance of the South American summer monsoon. *Mon. Wea. Rev.,* **133,** 663–676.

Moorthi, S., and M. J. Suarez, 1992: Relaxed Arakawa–Schubert: A parameterization of moist convection for general circulation models. *Mon. Wea. Rev.,* **120,** 978–1002.

Murakami, M., 1979: Large-scale aspects of deep convective activity over the GATE area. *Mon. Wea. Rev.,* **107,** 994–1013.

Nogués-Paegle, J., and K.-C. Mo, 1997: Alternating wet and dry conditions over South America during summer. *Mon. Wea. Rev.,* **125,** 279–291.

——, and Coauthors, 2002: Progress in Pan American CLIVAR research: Understanding the South American monsoon. *Meteorologica,* **27,** 3–30.

Nordeng, T. E., 1994: Extended versions of the convective parameterization scheme at ECMWF and their impact on the mean and transient activity of the model in the tropics. Tech. Memo. 206, European Centre for Medium-Range Weather Forecasts, Reading, United Kingdom, 41 pp.

Paegle, J. N., L. A. Byerle, and K. C. Mo, 2000: Intraseasonal modulation of South American summer precipitation. *Mon. Wea. Rev.,* **128,** 837–850.

Pan, D.-M., and D. A. Randall, 1998: A cumulus parameterization with a prognostic closure. *Quart. J. Roy. Meteor. Soc.,* **124,** 949–981.

Russell, G. L., J. R. Miller, and D. Rind, 1995: A coupled atmosphere–ocean model for transient climate change studies. *Atmos.–Ocean,* **33** (4), 683–730.

Tiedtke, M., 1989: A comprehensive mass flux scheme for cumulus parameterization in large-scale models. *Mon. Wea. Rev.,* **117,** 1779–1800.

Tokioka, T., K. Yamazaki, A. Kitoh, and T. Ose, 1988: The equatorial 30-60-day oscillation and the Arakawa-Schubert penetrative cumulus parameterization. *J. Meteor. Soc. Japan,* **66,** 883–901.

Torrence, C., and G. P. Compo, 1998: A practical guide to wavelet analysis. *Bull. Amer. Meteor. Soc.,* **79,** 61–78.

Turner, A. G., P. M. Inness, and J. M. Slingo, 2005: The role of the basic state in the ENSO-monsoon relationship and implications for predictability. *Quart. J. Roy. Meteor. Soc.,* **131,** 781–804.

Vera, C., and Coauthors, 2006a: Toward a unified view of the American monsoon systems. *J. Climate,* **19,** 4977–5000.

——, G. Silvestri, B. Liebmann, and P. González, 2006b: Climate change scenarios for seasonal precipitation in South America from IPCC-AR4 models. *Geophys. Res. Lett.,* **33,** L13707, doi:10.1029/2006GL025759.

Webster, P. J., 1983: Mechanisms of monsoon low-frequency variability: Surface hydrological effects. *J. Atmos. Sci.,* **40,** 2110–2124.

Wheeler, M., and G. N. Kiladis, 1999: Convectively coupled equatorial waves: analysis of clouds and temperature in the wavenumber–frequency domain. *J. Atmos. Sci.,* **56,** 374–399.

Zhang, G. J., and N. A. McFarlane, 1995: Sensitivity of climate simulations to the parameterization of cumulus convection in the CCC-GCM. *Atmos.–Ocean,* **3,** 407–446.

Zhou, J., and W. K.-M. Lau, 1998: Does a monsoon climate exist over South America? *J. Climate,* **11,** 1020–1040.